Enabling High-performance NASICON-based Solid-state Lithium Metal Batteries towards Practical Conditions

Andrea Paolella,* Xiang Liu, Amine Daali, Wenqian Xu, Inhui Hwang, Sylvio Savoie, Gabriel Girard, Alina Gheorghe Nita, Alexis Perea, Hendrix Demers, Wen Zhu, Abdelbast Guerfi, Ashok Vijh, Giovanni Bertoni, Gian Carlo Gazzadi, Giulia Berti, Chengjun Sun, Yang Ren, Karim Zaghib, Michel Armand, Chisu Kim, Gui-Liang Xu* and Khalil Amine*

Dr. A. Paolella, Dr. S. Savoie, Dr. G. Girard, Dr. A. G. Nita, Dr. A. Perea, Dr. H. Demers, Dr. W. Zhu, Dr. A. Guerfi, Dr. A. Vijh, Dr. K. Zaghib, Dr. C. Kim

Hydro-Québec, Center of Excellence in Transportation Electrification and Energy Storage, Varennes, Québec J0L 1N0, Canada

E-mail: Paolella.andrea2@hydro.qc.ca

Dr. X. Liu, Dr. A. Daali, Dr. G. L. Xu, Dr. K. Amine
Chemical Sciences and Engineering division, Argonne National Laboratory, 9700 South Cass Avenue, Lemont, IL 60439, USA

E-mail: xug@anl.gov (G.X.); amine@anl.gov (K.A.)

Dr. W. Xu, Dr. I. Hwang, Dr. C. J. Sun, Dr. Y. Ren

X-ray Science Division, Argonne National Laboratory, 9700 South Cass Avenue, Lemont, IL 60439, USA

Dr. G. Bertoni, Dr. G. Gazzadi

Istituto Nanoscienze-Consiglio Nazionale delle Ricerche, Via Giuseppe Campi, 213, 41125 Modena, Italy

Dr. G. Berti

INRS, Centre Énergie Matériaux Télécommunication, 1650, boulevard Lionel-Boulet, Varennes (Québec) J3X 1S2, Canada

Dr. K. Zaghib

Department of Mining and Materials Engineering, McGill University, Wong Building, 3610 University Street, Montreal, QC, H3A OC5, Canada

Dr. M. Armand

CIC Energigune, Parque Tecnológico de Álava, Albert Einstein, 48, 01510 Vitoria-Gasteiz, Álava, Spagna

Dr. K. Amine

Materials Science and Engineering, Stanford University, Stanford, CA, USA

WILEY-VCH

Solid-state lithium metal batteries (SSLMBs) are promising next-generation high-energy rechargeable batteries. However, the practical energy densities of the reported SSLMBs have been significantly overstated due to the use of thick solid-state electrolytes, thick lithium (Li) anode and thin cathodes. Here, a high-performance NASICON-based SSLMB using a thin (60 μm) $Li_{1.5}Al_{0.5}Ge_{1.5}(PO_4)_3$ (LAGP) electrolyte, ultrathin (36 μm) Li metal and high-loading (8 mg/cm^2) $LiFePO_4$ (LFP) cathode is reported. The thin and dense LAGP electrolyte prepared by hot-pressing exhibits a high Li ionic conductivity of 1×10^{-3} S cm^{-1} at 80° C. The assembled SSLMB can thus deliver an increased areal capacity of ~1 mAh/cm^2 at C/5 with a high capacity retention of ~ 96% after 50 cycles under 80 ^{o}C. Furthermore, it is revealed by synchrotron X-ray absorption spectroscopy and in situ high-energy X-ray diffraction that the side reactions between LAGP electrolyte and LFP cathode are significantly suppressed, while rational surface protection is required for Ni-rich layered cathodes. This study provides valuable insights and guideline for the development of high-energy SSLMBs towards practical conditions.

With increasing energy demand on the portable electronic devices and electric vehicles, the development of lithium-ion batteries (LIBs) with higher-energy-density is essential. Lithium is the ultimate anode that can dramatically boost the energy density of lithium batteries.[1] However, current liquid electrolytes are flammable and will trigger the formation of lithium dendrite during cycling, leading to severe safety concern and deteriorated cycle stability.[2] Solid-state lithium metal batteries (SSLMBs) using solid-state electrolytes (SSEs) have been considered as promising next generation rechargeable batteries because of their increased energy density and improved safety performance over existing LIBs.[3] Various types of SSEs have been reported, including solid polymer electrolytes (SPEs), sulfides-based, halides-based and oxide-based SSEs.[4] Among them, SPEs suffer from poor ionic conductivity at room temperature, limited stability towards oxidation, despite easy processing,[5] while sulfides and halides are sensitive to moisture, limiting their practical application.[6, 7]

Oxides SSEs, including NASICON-type, perovskite-type and garnet-type have attracted significant interest because they possess the advantages of high ionic conductivity, good oxidation/thermal stability, and excellent mechanical strength as well as better moisture stability than sulfides and halides.[8] In recent years, oxide SSEs have been successfully implemented with $LiFePO_4$ (LFP),[9-22] $LiCoO_2$ (LCO)[23-26] and $LiNi_xCo_yMn_{1-x-y}O_2$ (NCM)[14, 27-31] cathodes and demonstrated comparable specific capacity and cycle stability with that in the conventional liquid electrolytes. Deng et al. reported a Li/LFP battery using Li_3PO_4-coated $Li_{6.5}La_3Zr_{1.5}Ta_{0.5}O_{12}$ (LLZTO) electrolyte, which delivered a specific capacity of ~ 130 mAh/g at 1.5 C for 400 cycles.[11] Chen et al. designed a Au-LLZTO-PCE SSE for Li/LFP battery, which demonstrated a high specific capacity of 164 mAh/g with a stable cycle life up to 300 cycles.[17] These studies provide valuable guidelines for the design and fabrication of durable SSLMBs. However, the practical energy densities of the reported SSLMBs based on the configuration in **Figure 1**a were in fact very low, making them hard to compete with current LIBs. This is because the thickness of these oxide-based SSEs was typically over 0.5 mm, which not only increased the internal resistance and the manufacturing cost, but also significantly decreased the gravimetric/volumetric energy density. According to the simulation from Sun's group[4] and Huang's group[5], an oxide-based SSE with 0.5 mm thickness resulted in a low practical gravimetric energy density of < 50 Wh/kg for SSLMBs regardless of cathode specific capacity (from LFP to NCM to sulfur). This is because the inactive but thick SSEs account for over 70 wt.% weight of the whole SSLMB cell.[4] Therefore, reducing the thickness of SSEs is urgently required for practical SSLMBs.

Benefiting from advanced manufacturing, the fabrication of thin SSEs (< 100 μm) has been realized by using solution/slurry casting, tape-casting, hot/cold pressing and etc.[4] Recently, Peng and co-workers synthesized a thin $Li_{1+x}Al_xTi_{2-x}(PO_4)_3$ (88 μm) film for Li/LFP battery using

4

WILEY-VCH

hydrothermal approach, which enabled a specific capacity of 130 mAh/g for up to 30 cycles.[10] Jiang et al. reported a Li/PEO-LLTO-PEO/LFP battery with an ultrathin LLTO SSE (41 μm) by tape-casting, which delivered a specific capacity of 150 mAh/g at 0.1C for 50 cycles.[9] However, the areal cathode active material loadings in both works were only ~ 2 mg/cm^2, corresponding to an areal capacity loading of ~ 0.3 mAh/cm^2. Moreover, most of the literature work used thick Li metal (>0.5 mm) to pair with thin cathodes.[9-11, 13, 15, 17, 20, 21] Both of them will dramatically decrease the practical energy density of SSLMBs. **Table 1**, Figure 1c and 1d summarize the cell parameters of the reported SSLMBs using oxide-based SSEs, which clearly show that an SSLMB configuration based on thin oxide SSE, thin Li metal and thick cathode (Figure 1b) to enable high practical energy density has yet to be reported.

It has been shown that NASICON-type SSEs deliver higher energy density than perovskite-type and garnet-type under the same thickness due to their lower specific gravities.[9] For the consideration of energy density, here we fabricated a thin (60 μm) and densified self-standing NASICON-type $Li_{1.5}Al_{0.5}Ge_{1.5}(PO_4)_3$ (LAGP) SSE by using a novel sacrificial polycarbonate binder to avoid the formation of residual side products during hot-pressing, which possessed a high ionic conductivity of 1×10^{-3} S cm^{-1} at 80 °C. The assembled SSLMB using ultrathin Li anode (36 μm), thin LAGP electrolyte and dense LFP cathode with a high areal loading of 8 mg/cm^2 delivered a specific capacity of ~ 120 mAh/g after 50 cycles at 80 ^{o}C with a high capacity retention of ~96%. Synchrotron X-ray absorption spectroscopy (XAS) and in situ high-energy X-ray diffraction (HEXRD) characterization indicated that the excellent cell performance is attributed to the significantly suppressed parasitic reactions between LAGP electrolyte and LFP cathode.

5

LFP was selected as cathode material due to its low cost, source abundance, and unsurpassed safety as well as promising pack energy density.[32] The fabrication process of the LAGP/LFP-LAGP pellet by using a sacrificial polycarbonate binder was shown in Figure S1a. Hot pressing has been used to fabricate thin SSEs by heating the mixtures of SSEs and polymer binder, in which the binder was molten to enhance the flexibility of SSEs.[33] However, the addition of conventional binders will decrease the ionic conductivity of SSEs because they would form residual products after hot pressing. In this work, we used a volatile polycarbonate binder during the densification of LAGP and LAGP-LFP cathode pellet because it can completely decompose and form volatile cycling carbonate species during hot-pressing (Figure S1b).[34, 35] Therefore, it will not leave any residual products after hot pressing and can therefore increase the densification and ionic conductivity of the pellet. As shown in **Figure 2**a, the self-standing SSE film composed by LAGP electrolyte and polycarbonate polymer before hot pressing exhibited high porosity (marked with purple/pale blue contrast in Back Scattering Electron image). After hot pressing at a temperature of 650° C and a pressure of 56 MPa, it produced dense LAGP SSE with very little porosity of < 10% (Figure 2b). The total ionic conductivity of thin LAGP disk was measured to be 1.4×10^{-4} S cm^{-1} at room temperature and 1×10^{-3} S cm^{-1} at 80° C (Figure 2c). These numbers are one magnitude higher than that of our previously developed LAGP SSE using PVDF as sacrificial binder,[36] which formed residual carbonaceous products after hot pressing. The densification process was able to further fabricate a thin LAGP-LFP pellet with a total thickness of below 100 μm. Atomic Force Microscopy (Figure S2) image of pellet surface shows the result of melting process that occurred to LAGP nanoparticles after hot pressing step. Figure 2d shows clearly the cross-section dark-field SEM image of the LAGP-LFP pellet, which exhibited a flat LAGP layer with a thickness of 60 μm and a flat cathode layer (30 μm) on the top of graphite foil. The

EDS mapping in Figure 2e further shows the uniform distribution of Ge in the LAGP layer, Ge and Fe in the cathode layer. Moreover, there is no visible gap between LAGP and LFP cathode layer, indicating a good physical contact between them. This can significantly reduce the interfacial resistance and enhance the transport of Li$^+$ in the SSLMB.

Li/ionic-liquid interlayer/LAGP/LFP SSLMBs were then assembled by using the aforementioned LFP-LAGP pellet and a thin Li metal (36 μm) in coin-cells, in which the thickness of LAGP and Li metal are both very thin compared to many previous reports (Figure 1d). The areal LFP material loading in the electrodes were controlled at ~ 8 mg/cm^2, which is higher than many previously reported SSLMBs using LFP cathodes (Figure 1c). A 20 μm thick ionic-liquid interlayer consisting of LAGP, polycarbonate and Pyr13TFSI ionic liquid was inserted between half-cell and lithium metal to avoid side reactions (see Methods Section), which remains quasi-solid at a temperature up to ~ 140 ^{o}C (Figure S3 & S4). This is different from the previously reported approach by directly adding liquid electrolytes during cell fabrication and testing.[37] The use of LAGP/ionic-liquid interlayer is critical to the cell performance as confirmed by a comparison with that using a different LiTFSI/PEO interlayer (Figure S5): the lower coulombic efficiency observed for cell with IL:LAGP:QPAC interlayer (≥ 95%) with respect to the one with PEO (≥ 99%) could be due to polycarbonate binder reduction at lithium metal interface during charge process. The cells were tested within 2.5-4.0 V at 80 ^{o}C and the electrochemical performance were shown in **Figure 3**. Figure 3a shows the cycle performance of the Li/ionic-liquid interlayer/LAGP/LFP cell at a charge/discharge rate of C/5, while the inset shows the corresponding charge/discharge curves. The cell was under formation at C/24 and C/10 for two cycles, which delivered a reversible capacity of 135 mAh/g and 130 mAh/g, respectively. When increasing the rate to C/5, the specific capacity was stabilized at ~ 120 mAh/g after 50 cycles,

WILEY-VCH

corresponding to a high areal capacity loading of ~1.0 mAh/cm^2. Compared to most of the previously reported SSLMBs using oxide-based SSEs (Figure 1c and Table 1), our areal cathode capacity loading represents a considerable improvement. Figure 3b shows the electrochemical impedance spectroscopy of the cell after different cycles. The result clearly showed that there is no visible increase in the internal resistance, which remained a small value of < 100 Ω. The results indicated that there are no significant interfacial impediments or barriers for the ion migration in the cells. This is indirectly confirmed by Figure 2c in which the temperature dependence of conductivity is plotted. An estimate of the activation energy (strictly speaking apparent heat of activation) is around 16.62 kilojoules per mole, which is about 4 kcal per mole. Such a low value is characteristic of a diffusion process, rather than an activation-controlled charge transfers across the interfaces. Such diffusion-controlled rate-determining- step (rds) is consistent with the impedance curves in Figure 3b in which the usual semi-circles associated with charge transfer impedance are absent. Instead, one only gets straight lines, indicating again a diffusion-controlled process as the rds in this region. We further increased the charge/discharge rate to C/3, which can still maintain a reversible capacity of ~ 110 mAh/g with a high capacity retention of ~ 96% after 60 cycles (Figure 3c), demonstrating excellent cycle stability at elevated charge/discharge rate. The rate capability was also tested (Figure 3d), which delivered a specific capacity of 133.0 mAh/g, 127 mAh/g, 120 mAh/g, 111.8 mAh/g, 93.5 mAh/g and 65.6 mAh/g at C/24, C/12, C/6, C/3, 1C and 2C, respectively. Such rate performance surpassed recent report by Jiang et al. on the Li/LLTO/LFP SSLMB cell using thin LLTO (41 μm) and thin LFP (2 mg cm^{-2}) cathode in terms of specific capacity and areal capacity loading.[9] The cell showed slightly different voltage curve at low charge/discharge rate, which might be related to the formation of $Li_3Fe_2(PO_4)_3$ during hot-pressing.[38] Nevertheless, the combination of increased areal

8

capacity, thin LAGP and thin Li metal could thus result in a significant increase of the practical energy density. We further tested the cell at a lower temperature of 60° C. The cell could deliver a specific capacity of around 129 mAh/g at C/24, 119 mAh/g at C/10 and 110 mAh/g at C/5 (Figure S6). However, when cycled at room temperature, the cell exhibited much lower specific capacities during cycling (Figure S7), which should be related to the decreased ionic conductivity of LAGP at room temperature and insufficient mechanical bonding between LFP and LAGP,[38] and hence requires further rational interface engineering to reduce the operation temperature.

To unravel the origin for the stable cycle life of the above Li/ionic-liquid interlayer/LAGP/LFP SSLMB, we further conducted synchrotron XAS to reveal the local geometry and electronic structure changes of LAGP SSE and LFP cathode after cycling. **Figure 4a** shows the Ge K-edge X-ray absorption near edge spectroscopy (XANES) spectra of LAGP electrolyte before and after cycling for 50 cycles, which can provide the oxidation state information for Ge in the LAGP during cycling. As shown, there was no obvious edge shift or intensity decrease after repeated charge/discharge, indicating the structure of LAGP electrolyte was well maintained. We further conducted the extended X-ray absorption fine structure (EXAFS) analysis on the pristine and cycled LAGP to reveal the local structure changes. As shown in Figure 4b, no visible intensity decrease for the magnitudes of the first, second, and third peaks can be observed, indicating no formation of new phases and no breakdown of crystallinity inside LAGP electrolyte. The results indicate that there were limited parasitic reactions between LAGP and Li metal or LFP cathode during charge/discharge. Figure 4c and 4d display the Fe K-edge XANES and EXAFS spectra of LFP cathode before and after cycling with a referenced Fe foil, respectively. As shown in Figure 4c, no significant change in the Fe K-edge XANES can be seen, indicating limited structural changes on the cycled LFP in comparison with the

WILEY-VCH

pristine one. In the Fe K-edge EXAFS, the pristine LFP exhibited obvious Fe-O, Fe-P and Fe-Fe bond, which can be all well maintained even after 50 cycles of charge/discharge.

In situ heating on the cathode materials and liquid electrolytes have been widely used to predict their reactivity and correlate with their electrochemical performance and safety performance.[39] As reported by Hu et al.,[40] temperature can trigger similar structural degradation to battery materials as that during electrochemical cycling, but at a much faster speed (within hours). Thus, to further explore the interfacial stability between LFP cathode and LAGP electrolyte, we conducted in situ HEXRD characterization on the LFP/LAGP (50/50, w/w) mixture during heating from room temperature to 800 $^\circ$C followed by holding at 800 $^\circ$C for 9 h and then naturally cooling, which can monitor their interfacial reaction under high-temperature calcination. **Figure 5**a and 5b show the in situ HEXRD patterns and the corresponding contour plot of the LFP/LAGP mixture, respectively. Upon heating, the 2-theta position of LAGP peak (012) and LFP peaks (200, 210 and 011) all shifted to lower angles due to thermal expansion. During holding at 800 $^\circ$C for 9 h, no visible phase transition nor intensity decrease can be observed. During the cooling process, the peaks of both LAGP and LFP shifted towards higher angles due to thermal contraction, and then returned to their original 2-theta position after cooling down to room temperature, indicating a highly reversible crystal structure evolution during heating/cooling. The Rietveld refinement in Figure S8 showed that both pristine and cooled samples can be well refined by standard LAGP and LFP. In addition, the cell unit parameters for LAGP and LFP undergo less than 0.2% change during this process. The results clearly confirmed the superior stability of LAGP against LFP cathode, which should account for the good electrochemical performance of the assembled SSLMB. The cross-section SEM image of cycled cell showed that there is no separation at the LFP-LAGP interface (Figure S9), confirming no

10

WILEY-VCH

occurrence of structural fracture and limited parasitic reactions between them during cycling. HEXRD pattern of cycled LFP-LAGP pellet confirmed no formation of new phase after repeated cycling (Figure S10).

In order to further increase the energy density of SSLMB, coupling LAGP electrolytes with high-capacity cathodes such as NCM811 is required. We therefore probed the interfacial reactivity between LAGP electrolyte and conventional polycrystalline NCM811 cathode by conducting the same *in situ* heating on the LAGP/NCM811 (50/50, w/w) mixture. Figure 5c shows the corresponding contour plot of in situ HEXRD patterns during heating from room temperature to 800 $^{\circ}$C, which clearly revealed the occurrence of phase transition at high temperature. Figure 5d zoomed in the in situ HEXRD patterns in the temperature range of 600-800 $^{\circ}$C. The intensities of LAGP and NCM811 cathode were gradually decreased and completely disappeared at ~ 760 $^{\circ}$C, followed by the formation of a series of new peaks. These peaks can be well assigned to the $(Ni,Co,Mn)_3(PO_4)_2$ with P21/n space group. Such phase transition should come from the high reactivity between LAGP and NCM811, which would decrease the ionic transport at the interface and thus deteriorate the cell performance of Li/LAGP/NCM811 SSLMB during cycling. Future work will be focused on rational surface protection on either LAGP electrolyte or Ni-rich NCM cathodes to enable the deployment of high areal loading Ni-rich NCM cathodes in the practical SSLMBs.[41-43]

Reducing the thickness of solid-state electrolytes/lithium metal anode and increasing the areal cathode active material loading are essential to increase the practical energy density of SSLMBs. By using a volatile binder during hot-pressing, we have successfully fabricated a thin and dense LAGP SSE, which increased the ionic conductivity to 1×10^{-3} S cm^{-1} at 80° and hence significantly facilitated the transport of Li$^+$ and decreased the internal cell resistance. When further coupling with an

11

WILEY-VCH

ultrathin (36 μm) Li metal and high-loading LFP cathode, the fabricated solid-state cell demonstrated significantly improved areal capacity and cycle stability over many previously reported SSLMBs using oxide-based SSEs. Such excellent electrochemical performance was attributed to the limited side reactions between LAGP and LFP cathode as revealed by synchrotron X-ray characterization. The present work is a good demonstration on the development of SSLMBs under practical conditions, which will promote the advance of SSLMBs with high practical energy density.

Experimental Section

Materials: LAGP was purchased from MSE (USA), the typical granular particle size distribution (PSD) was D10/ μm = 0.342; D50/ μm= 0.512; D90/ μm=0.769. LiFePO$_4$@C was purchased from Sumitomo with a narrow particle size distribution (D50/ μm =0.140), while graphite was purchased from Hitachi. Ionic Liquid Pyr13-TFSI was purchased from Solvionic. LiTFSI was purchased from Solvay while polycarbonate QPAC 25 was purchased from Empower with a molecular weight MW from approximately 50,000 to 200,000. Hot pressing was performed in an argon-filled hot press that was purchased from OxyGon (New Hampshire, USA).

Solid electrolyte and cathode thin film fabrication: The solid electrolyte slurry was prepared in a dry room by mixing LAGP (95% w/w) and polycarbonate binder (5% w/w) with DMF-THF (1/1, v/v) in a Thinky machine for 10 minutes (International Patent: WO/2020/223799). The slurry was then coated on polypropylene film and dried at 50 °C for 10-15 minutes. To prepare the cathode thin film, LiFePO$_4$@C was mixed with LAGP and graphite at an optimal weight ratio of 50:45:5 (see Figure S11 for a comparison with different ratio). The mixture (95% w/w) was further mixed with polycarbonate

binder (5% w/w) and NMP in Thinky machine for 10 minutes. The slurries were coated on polypropylene films and then dried at 50 °C. The areal $LiFePO_4$ loading in the electrodes was controlled at ~ 8 mg cm^{-2}.

Electron microscopy and chemical mapping: Scanning transmission electron microscopy images were acquired using an annular dark field mode (ADF-STEM) on a JEM-2200FS transmission electron microscope operated at 200 kV (JEOL, Japan). Chemical mapping was performed using an energy dispersive X-ray spectrometer (EDXS) in the scanning mode. The cross section were prepared using an Ar Ion Milling IM4000 Plus (Hitachi, Japan) with a ion beam energy of 6 kV with a fast and 30 º rotation for 4 hours. The cross section surfaces were analyzed using scanning electron microscope (SEM) Lyra 3 (TESCAN) and elemental composition obtained using windowless energy dispersive spectrometer (EDS) Extreme (Oxford instruments). The micrograph and x-ray map were acquired at an accelerating voltage of 5 and 10 kV, a probe current of 500 pA, and a working distance of 10 mm. The phase distribution in Figure 2 was obtained from a compositional (BSE) image and the pixel intensity. A range of pixel intensity is manually selected for each phase and the Tescan software tool Object Area calculate the image pixel fraction of each phase and a phase image.

Synchrotron HEXRD and XAS characterization: In situ synchrotron high-energy XRD characterization during heating were conducted at Beamline 11-ID-C and 17-BM of the Advanced Photon Source (APS) at Argonne National Laboratory. The X-ray wavelength in 11-ID-C and 17-BM were 0.1173 Å and 0.24117 Å, respectively. The 2-theta was normalized to the same wavelength (0.1173 Å). By using the FIT2D program calibrated against a CeO_2 standard, we converted 2D images into a 1D plot of 2θ versus intensity. $LiFePO_4$ powder was mixed with LAGP powder with an weight ratio of 50/50. As a comparison, $LiNi_{0.8}Co_{0.1}Mn_{0.1}O_2$ powder was mixed with LAGP powder with the same weight

ratio. The mixtures were pressed into a pellet with a diameter of 7 mm before *in situ* heating. The samples were heated to 800 °C in a TS-1500 furnace with a constant heating rate of 5 °C min^{-1}. HEXRD patterns were continuously collected during the course of the experiment. Ge K-edge and Fe K-edge XAS of pristine and cycled LAGP were carried out in transmission mode at Beamline 20-BM-B of the APS.

Ionic conductivity: In order to perform the electrical conductivities measurements, we hot pressed a self-standing thin LAGP self-standing electrolyte on graphite. After densification at 650 °C, the electrolyte was sandwiched between two graphite disk in coin cell. The electrical conductivity of the sample was calculated taking into account the dimensions and the distance between the electrodes and the values of resistance (Ω) obtained.

Battery preparation and testing: the self-standing films of cathode and solid electrolyte were punched in disk of 16 mm of diameter (corresponding to an area of 2 cm^2). Then, the two disks were hot-pressed in Argon-filled hot press by applying a pressure of 56 MPa and 650 °C for 1 hour. The final disks were assembled with thin metallic lithium (36 µm thick-Hydro-Québec) in the Ar-filled glove box, in which a 20 µm interlayer was inserted between them to prevent side reactions between Li and LAGP. Then the battery was cycled in 2032 coin cell at 80 °C. The ionic-liquid interlayer was prepared by coating a slurry consisting of LAGP (60% w/w) of polycarbonate binder (15% w/w) in N-methyl pyrrolidone (NMP) followed by the addition of 1M LiTFSI in pyr13TFSI (25% w/w). A different 10 µm PEO:LiTFSI (EO:Li = 20:1, w/w) interlayer was also used between the LAGP and lithium (Figure S5). The Li//PEO-LiTFSI//LAGP//LFP-LAGP all-solid battery was prepared by hot pressing lithium metal and an LAGP//LFP-LAGP half-cell at 80 °C using a PEO-LiTFSI interlayer to protect the lithium metal from side reactions with LAGP.

WILEY-VCH

Supporting Information

Supporting Information is available from the Wiley Online Library or from the author.

Author contribution

G.X., A.P. and K.A. initiated and supervised the project. A.P. and S.S. designed the hot press experiments. X.L., G.X., A.D., W.X. and Y.R. conducted the in situ HEXRD experiments and analysis. X.L., G.X., I.H. and C.S. performed XAFS characterization and analysis. A.G.N. prepared the cathode and electrolyte thin film pellets. G.G. and A.P. performed electrochemical analysis. H.D., W.Z., G.B., and G.G. performed microscopy (SEM) experiments. G.B. performed AFM measurement. G.X. wrote the manuscript with the input from all authors.

WILEY-VCH

References

[1]   H. Duan, Y.-X. Yin, Y. Shi, P.-F. Wang, X.-D. Zhang, C.-P. Yang, J.-L. Shi, R. Wen, Y.-G. Guo, L.-J. Wan, *J. Am. Chem. Soc.* **2018**, 140, 82.

[2]   R. Amine, J. Liu, I. Acznik, T. Sheng, K. Lota, H. Sun, C.-J. Sun, K. Fic, X. Zuo, Y. Ren, D. A. Ei-Hady, W. Alshitari, A. S. Al-Bogami, Z. Chen, K. Amine, G.-L. Xu, *Adv. Energy Mater.* **2020**, 10, 2000901.

[3]   Q. Zhao, S. Stalin, C.-Z. Zhao, L. A. Archer, *Nat. Rev. Mater.* **2020**, 5, 229.

[4]   X. Yang, K. Adair, X. Gao, X. Sun, *Energy Environ. Sci.* **2021**, 14, 643-671.

[5]   J. Wu, L. Yuan, W. Zhang, Z. Li, X. Xie, Y. Huang, *Energy Environ. Sci.* **2021**, 14, 12-36.

[6]   S. Chen, D. Xie, G. Liu, J. P. Mwizerwa, Q. Zhang, Y. Zhao, X. Xu, X. Yao, *Energy Storage Mater.* **2018**, 14, 58.

[7]   W. Li, J. Liang, M. Li, K. R. Adair, X. Li, Y. Hu, Q. Xiao, R. Feng, R. Li, L. Zhang, S. Lu, H. Huang, S. Zhao, T.-K. Sham, X. Sun, *Chem. Mater.* **2020**, 32, 7019.

[8]   K. J. Kim, M. Balaish, M. Wadaguchi, L. Kong, J. L. M. Rupp, *Adv. Energy Mater.* **2020**, 2002689.

[9]   Z. Jiang, S. Wang, X. Chen, W. Yang, X. Yao, X. Hu, Q. Han, H. Wang, *Adv. Mater.* **2020**, 32, 1906221.

[10]   C. Peng, Y. Kamiike, Y. Liang, K. Kuroda, M. Okido, *Acs Sustain. Chem. Eng.* **2019**, 7, 10751.

[11]   T. Deng, X. Ji, Y. Zhao, L. Cao, S. Li, S. Hwang, C. Luo, P. Wang, H. Jia, X. Fan, X. Lu, D. Su, X. Sun, C. Wang, J.-G. Zhang, *Adv. Mater.* **2020**, 32, 2000030.

[12]   Y. Ruan, Y. Lu, Y. Li, C. Zheng, J. Su, J. Jin, T. Xiu, Z. Song, M. E. Badding, Z. Wen, *Adv. Funct. Mater.* **2020**, 2007815.

[13]   Q. Zhou, B. Xu, P.-H. Chien, Y. Li, B. Huang, N. Wu, H. Xu, N. S. Grundish, Y.-Y. Hu, J. B. Goodenough, *Small Methods* **2020**, 4, 2000764.

[14]   Y. Ruan, Y. Lu, X. Huang, J. Su, C. Sun, J. Jin, Z. Wen, *J. Mater. Chem. A* **2019**, 7, 14565.

[15]   H. Xu, Y. Li, A. Zhou, N. Wu, S. Xin, Z. Li, J. B. Goodenough, *Nano Lett.* **2018**, 18, 7414.

[16]   Y. Zhong, Y. Xie, S. Hwang, Q. Wang, J. J. Cha, D. Su, H. Wang, *Angew. Chem. Int. Ed.* **2020**, 59, 14003.

[17]   S. Chen, J. Zhang, L. Nie, X. Hu, Y. Huang, Y. Yu, W. Liu, *Adv. Mater.* **2020**, 2002325.

[18]   F. Du, N. Zhao, Y. Li, C. Chen, Z. Liu, X. Guo, *J. Power Sources* **2015**, 300, 24.

[19]   S.-S. Chi, Y. Liu, N. Zhao, X. Guo, C.-W. Nan, L.-Z. Fan, *Energy Storage Mater.* **2019**, 17, 309.

WILEY-VCH

[20]   Y. Li, X. Chen, A. Dolocan, Z. Cui, S. Xin, L. Xue, H. Xu, K. Park, J. B. Goodenough, *J. Am. Chem. Soc.* **2018**, 140, 6448.

[21]   W. Luo, Y. Gong, Y. Zhu, Y. Li, Y. Yao, Y. Zhang, K. Fu, G. Pastel, C.-F. Lin, Y. Mo, E. D. Wachsman, L. Hu, *Adv. Mater.* **2017**, 29, 1606042.

[22]   Y. Meesala, C.-Y. Chen, A. Jena, Y.-K. Liao, S.-F. Hu, H. Chang, R.-S. Liu, *J. Phys. Chem. C* **2018**, 122, 14383.

[23]   H. Huo, Y. Chen, R. Li, N. Zhao, J. Luo, J. G. Pereira da Silva, R. Mücke, P. Kaghazchi, X. Guo, X. Sun, *Energy Environ. Sci.* **2020**, 13, 127.

[24]   F. Han, J. Yue, C. Chen, N. Zhao, X. Fan, Z. Ma, T. Gao, F. Wang, X. Guo, C. Wang, *Joule* **2018**, 2, 497.

[25]   S. Ohta, T. Kobayashi, J. Seki, T. Asaoka, *J. Power Sources* **2012**, 202, 332.

[26]   Z. Bi, N. Zhao, L. Ma, Z. Fu, F. Xu, C. Wang, X. Guo, *Chem. Eng. J.* **2020**, 387, 124089.

[27]   Z. Zhao, Z. Wen, X. Liu, H. Yang, S. Chen, C. Li, H. Lv, F. Wu, B. Wu, D. Mu, *Chem. Eng. J.* **2021**, 405, 127031.

[28]   T. Liu, Y. Zhang, X. Zhang, L. Wang, S.-X. Zhao, Y.-H. Lin, Y. Shen, J. Luo, L. Li, C.-W. Nan, *J. Mater. Chem. A* **2018**, 6, 4649.

[29]   Y. Shao, H. Wang, Z. Gong, D. Wang, B. Zheng, J. Zhu, Y. Lu, Y.-S. Hu, X. Guo, H. Li, X. Huang, Y. Yang, C.-W. Nan, L. Chen, *Acs Energy Lett.* **2018**, 3, 1212.

[30]   George V. Alexander, N. C. Rosero-Navarro, A. Miura, K. Tadanaga, R. Murugan, *J. Mater. Chem. A* **2018**, 6, 21018.

[31]   H. Duan, M. Fan, W.-P. Chen, J.-Y. Li, P.-F. Wang, W.-P. Wang, J.-L. Shi, Y.-X. Yin, L.-J. Wan, Y.-G. Guo, *Adv. Mater.* **2019**, 31, 1807789.

[32]   X.-G. Yang, T. Liu, C.-Y. Wang, *Nat. Energy* **2021**, 6, 176.

[33]   J. M. Whiteley, P. Taynton, W. Zhang, S.-H. Lee, *Adv. Mater.* **2015**, 27, 6922.

[34]   B. Commarieu, A. Paolella, S. Collin-Martin, C. Gagnon, A. Vijh, A. Guerfi, K. Zaghib, *J. Power Sources* **2019**, 436, 226852.

[35]   O. Phillips, J. M. Schwartz, P. A. Kohl, *Polym. Degrad. Stab.* **2016**, 125, 129.

[36]   A. Paolella, W. Zhu, G.-L. Xu, A. La Monaca, S. Savoie, G. Girard, A. Vijh, H. Demers, A. Perea, N. Delaporte, A. Guerfi, X. Liu, Y. Ren, C.-J. Sun, J. Lu, K. Amine, K. Zaghib, *Adv. Energy Mater.* **2020**, 10, 2001497.

[37]   E. Yi, H. Shen, S. Heywood, J. Alvarado, D. Y. Parkinson, G. Chen, S. W. Sofie, M. M. Doeff, *Acs Appl. Energy Mater.* **2020**, 3, 170.

[38]   K. J. Kim, J. L. M. Rupp, *Energy Environ. Sci.* **2020**, 13, 4930.

[39]   X. Liu, G.-L. Xu, L. Yin, I. Hwang, Y. Li, L. Lu, W. Xu, X. Zhang, Y. Chen, Y. Ren, C.-J. Sun, Z. Chen, M. Ouyang, K. Amine, *J. Am. Chem. Soc.* **2020**, 142, 19745.

[40]   E. Hu, X. Yu, R. Lin, X. Bi, J. Lu, S. Bak, K.-W. Nam, H. L. Xin, C. Jaye, D. A. Fischer, K. Amine, X.-Q. Yang, *Nat. Energy* **2018**, 3, 690.

[41]   A. Y. Kim, F. Strauss, T. Bartsch, J. H. Teo, T. Hatsukade, A. Mazilkin, J. Janek, P. Hartmann, T. Brezesinski, *Chem. Mater.* **2019**, 31, 9664.

[42]   F. Strauss, J. H. Teo, J. Maibach, A. Y. Kim, A. Mazilkin, J. Janek, T. Brezesinski, *Acs Appl. Mater. Interfaces* **2020**, 12, 57146.

[43]   X.-D. Zhang, J.-L. Shi, J.-Y. Liang, L.-P. Wang, Y.-X. Yin, K.-C. Jiang, Y.-G. Guo, *J. Power Sources* **2019**, 426, 242.
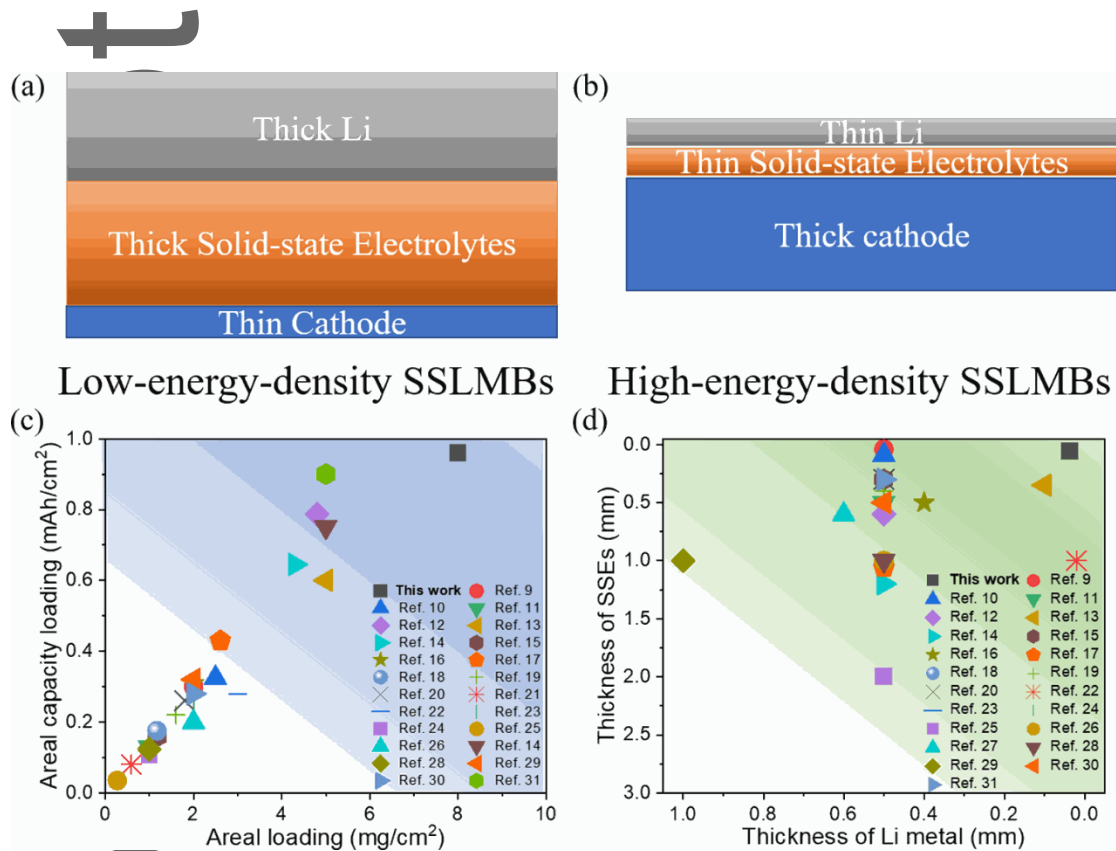
Figure 1. (a, b) Two SSLMB configurations based on different thickness of Li metal, SSE and cathode loading. (c) The comparison of areal capacity versus areal active material loading in SSLMBs in the literature; (d) The comparison on the thickness of Li metal and oxide-based SSEs in SSLMBs in the literature. The data in (c) and (d) are from Table 1.
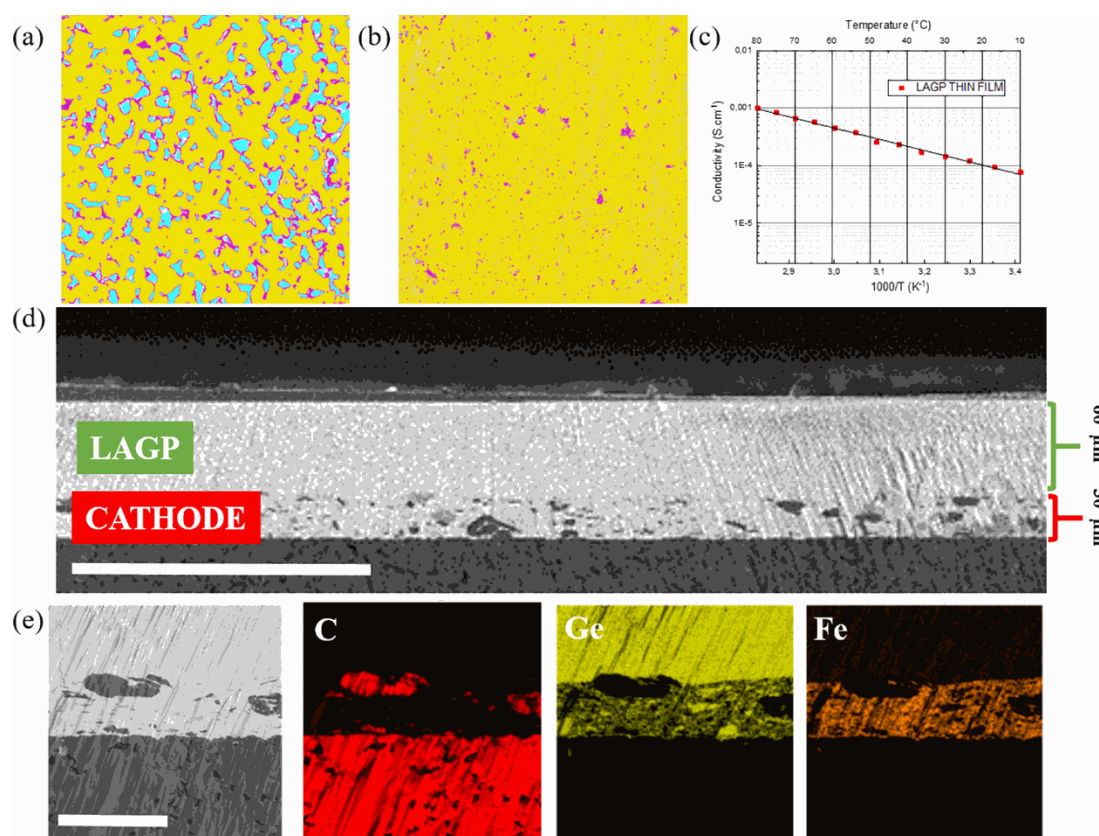
Figure 2. Cross section image of the LAGP (a) before and (b) after hot pressing; Scale bar is 5 µm; c) ionic conductivity measurement of LAGP thin film after hot pressing; (d) Cross-section SEM image of thin LGP-LAGP-graphite cathode/LAGP electrolyte and (e) EDS mapping. Scale bar in (d) and (e) are 200 µm and 50 µm, respectively.
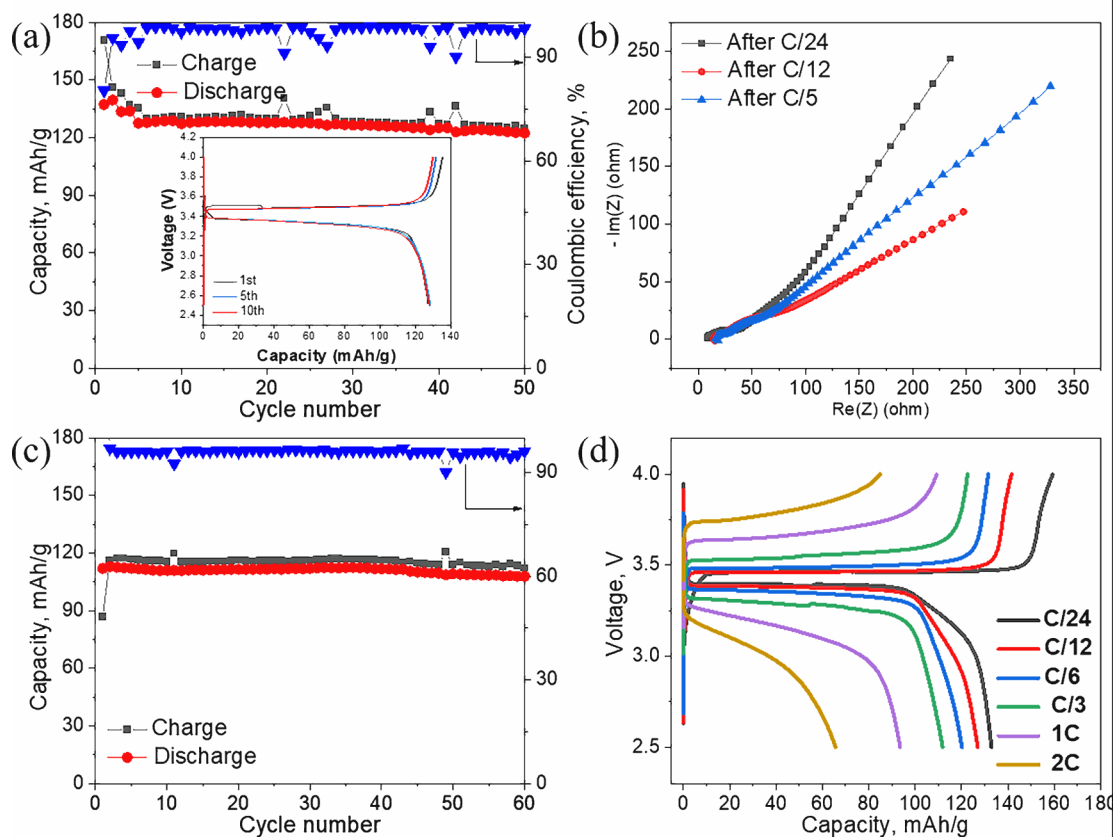
19

Figure 3. a) Cycling performance of Li/ionic-liquid interlayer/LAGP/LFP SSLMB at a charge/discharge rate of C/5 at 80° C, inset is the corresponding charge/discharge curves at C/5; b) Electrochemical impedance spectroscopy of Li/ionic-liquid interlayer/LAGP/LFP SSLMB after charge/discharge; c) Cycling performance of Li/ionic-liquid interlayer/LAGP/LFP SSLMB at a charge/discharge rate of C/3 at 80° C; d) rate capability of Li/ionic-liquid interlayer/LAGP/LFP SSLMB at 80° C.
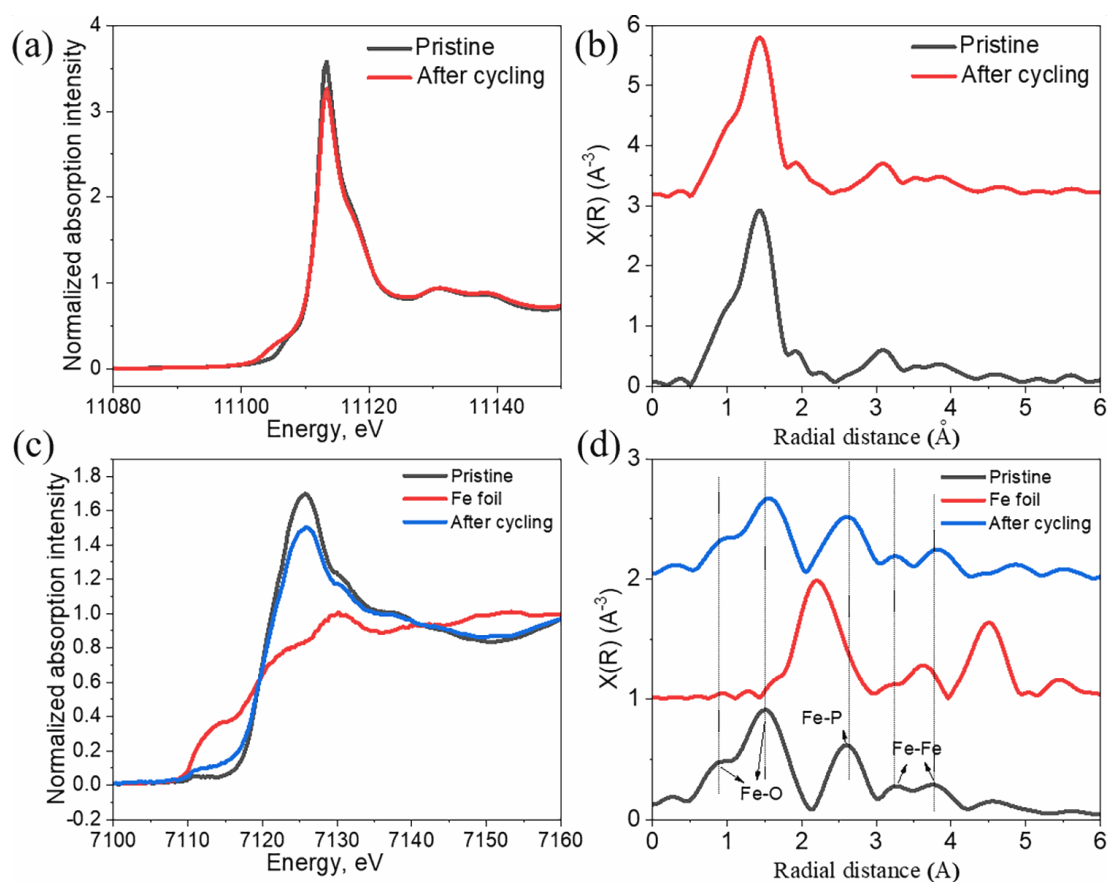
Figure 4. Ge K-edge XANES (a) and EXAFS (b) spectra of LAGP electrolyte before and after cycling; Fe K-edge XANES (a) and EXAFS (b) spectra of LFP cathode before and after cycling.
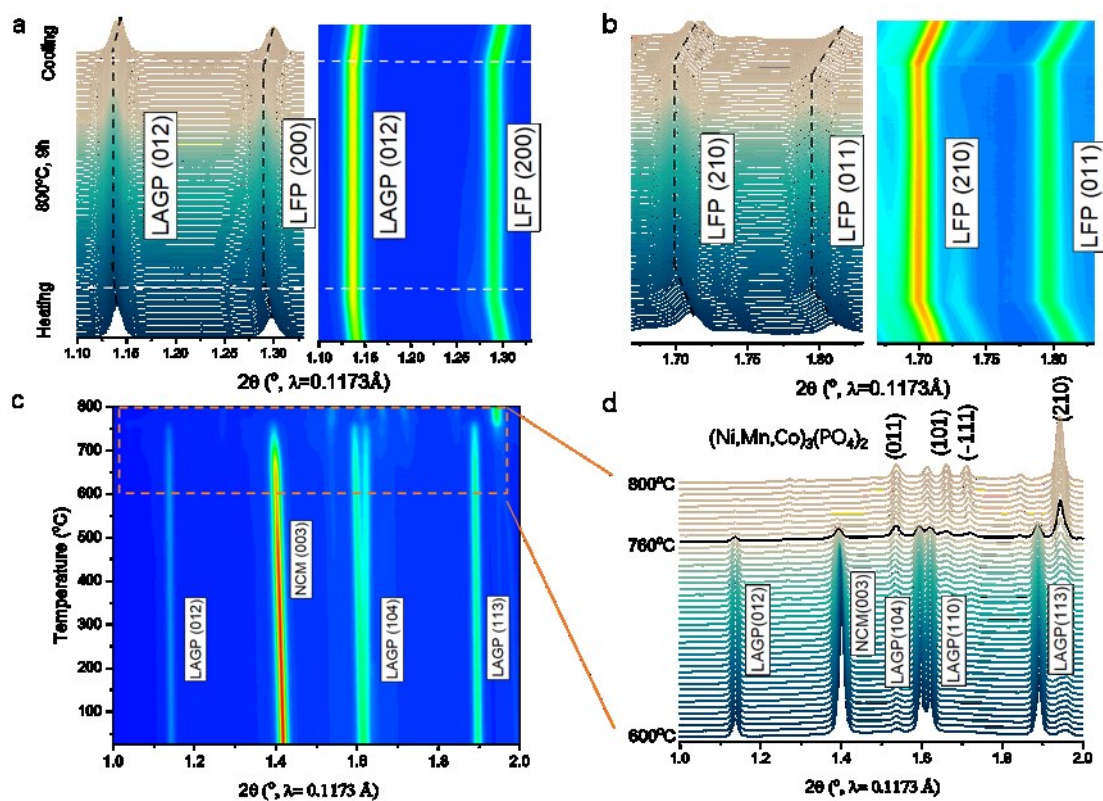
21

Figure 5. (a, b) In situ HEXRD patterns and the corresponding contour plot of LAGP/LFP mixture during heating and cooling; (c) Contour plot and (d) in situ HEXRD patterns of LAGP/NCM811 mixture during heating to 800 $^{\circ}$C.

22

Table 1 Literature review of solid-state lithium batteries based on oxides-type solid electrolytes.

Battery structure	Li thickness*	Thickness of SSEs (mm)	Working temperature (°C)	Current density (mA/cm^2)	Specific capacity (mAh/g)	Mass loading (mg/cm^2)	Areal capacity (mAh/cm^2)	Cycling life	[Ref]
Li/LAGP/LFP	0.036 mm	0.06	80	0.272	120	8	0.96	50	This work
Li/PEO-LLTO-PEO/LFP	unlimited Li	0.041	65	0.034	150	2	0.3	50	[9]
Li/LATP/LFP	unlimited Li	0.088	25	0.068-0.085	130	2-2.5	0.26-0.325	30	[10]
Li/LPO-LLZO/LFP	unlimited Li	0.5-0.8	25	0.1	~130	1	0.13	400	[11]
Li/LiF-LiCl-LLZT/LFP	unlimited Li	0.6-0.8	25	0.1	164.2	4.8	0.788	100	[12]
Li/$_{Li1+2x}$Mg$_x$Zr$_{2-x}$(PO$_4$)$_3$/LFP	0.1 mm	0.35	25	0.1	120	3-5	0.36-0.6	50	[13]
Li/Li$_3$PO$_4$-LLZTO/LFP	unlimited Li	1.2	25	0.095	150	4.3	0.645	100	[14]
Li/Li$_3$N-LLZO/LFP	unlimited Li	0.3	60	0.05	133	1.18	0.16	90	[15]
Li/LLZTO/LFP	0.4 mm	> 0.5	60	0.051-0.068	155	1.5-2.0	0.23-0.31	400	[16]
Li/LLZTO-PCE/LFP	unlimited Li	1.06	25	0.0444	164	2.61	0.43	300	[17]
Li/LLZTO/LFP	unlimited Li	1.0	60	0.05	150	1.17	0.175	100	[18]
Li/SPE-LLZTO-SPE/LFP	unlimited Li	0.4	90	0.0544	140	1.6	0.22	200	[19]
Li/LLZO/LFP	unlimited Li	0.3	65	0.1	143	1.2-1.8	0.17-0.26	100	[20]
Li/Ge/LLZO/GPE/LFP	unlimited Li	-	RT	0.1	138	0.59	0.08	100	[21]
Li/LAGP/LFP	0.02 mm	1-2	RT	0.017-0.0255	96	2-3	0.19-0.28	50	[22]

WILEY-VCH

Li/Cu$_3$N-LLZO/LCO	unlimited Li	1.0	25	0.024	125	2	0.25	300	[23]
Li/LCBO-LLZO/LCO	unlimited Li	1	100	0.00575	106	1	0.106	40	[24]
Li/LLZNbO/LCO	unlimited Li	2	25	0.0035	130	0.27	0.035	100	[25]
Li/LLZO-PP13-TFSI/LCO@LLZO	unlimited Li	1	60	0.046	~100	2	0.2	400	[26]
Li/Li$_3$PO$_4$-LLZTO/NCM523	unlimited Li	1.2	25	0.15	150	5	0.75	120	[14]
Li/Li$_3$PO$_4$-LLZTO/NCM811	0.6 mm	0.6	100	-	150	-	-	100	[27]
Li/LLZTO/NCM523	unlimited Li	1	80	0.005	123.3	1	0.123	5	[28]
Li/LALZWO/IL/NCM523	1 mm	1	80	~0.18	~160	2	0.32	500	[29]
Li/LLZO/Li2SiO3/NCM111	unlimited Li	0.5	100	0.01	138	2	0.28	10	[30]
Li/PAN-LAGP-PEGDA/NCM811	unlimited Li	0.3	RT	0.108-0.18	180	3-5	0.54-0.9	170	[31]

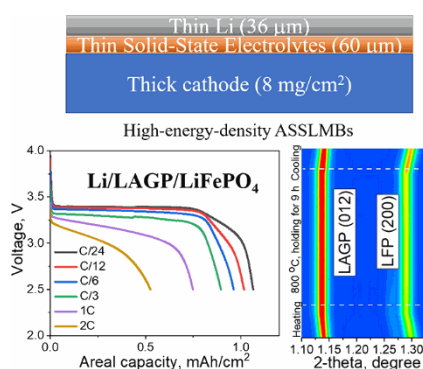***The thickness of Li metal that was not provided in the literature was defined as unlimited Li.**

WILEY-VCH

A solid-state lithium metal batteries using ultrathin Li metal anode, thin NASICON-based solid-state electrolytes and thick LiFePO$_4$ cathode towards practical application is developed. Moreover, such cell design significantly decreases the internal cell resistance and mitigates the parasitic reactions between cathode and solid electrolytes, thus demonstrating excellent cycle stability and rate capability with high areal capacity.

Andrea Paolella, *Xiang Liu, Amine Daali, Wenqian Xu, Inhui Hwang, Sylvio Savoie, Gabriel Girard, Alina Gheorghe Nita, Alexis Perea, Hendrix Demers, Wen Zhu, Abdelbast Guerfi, Ashok Vijh, Giovanni Bertoni, Gian Carlo Gazzadi, Giulia Berti, Chengjun Sun, Yang Ren, Karim Zaghib, Michel Armand, Chisu Kim, Gui-Liang Xu* and Khalil Amine**

Enabling High-performance NASICON-based Solid-state Lithium Metal Batteries towards Practical Conditions